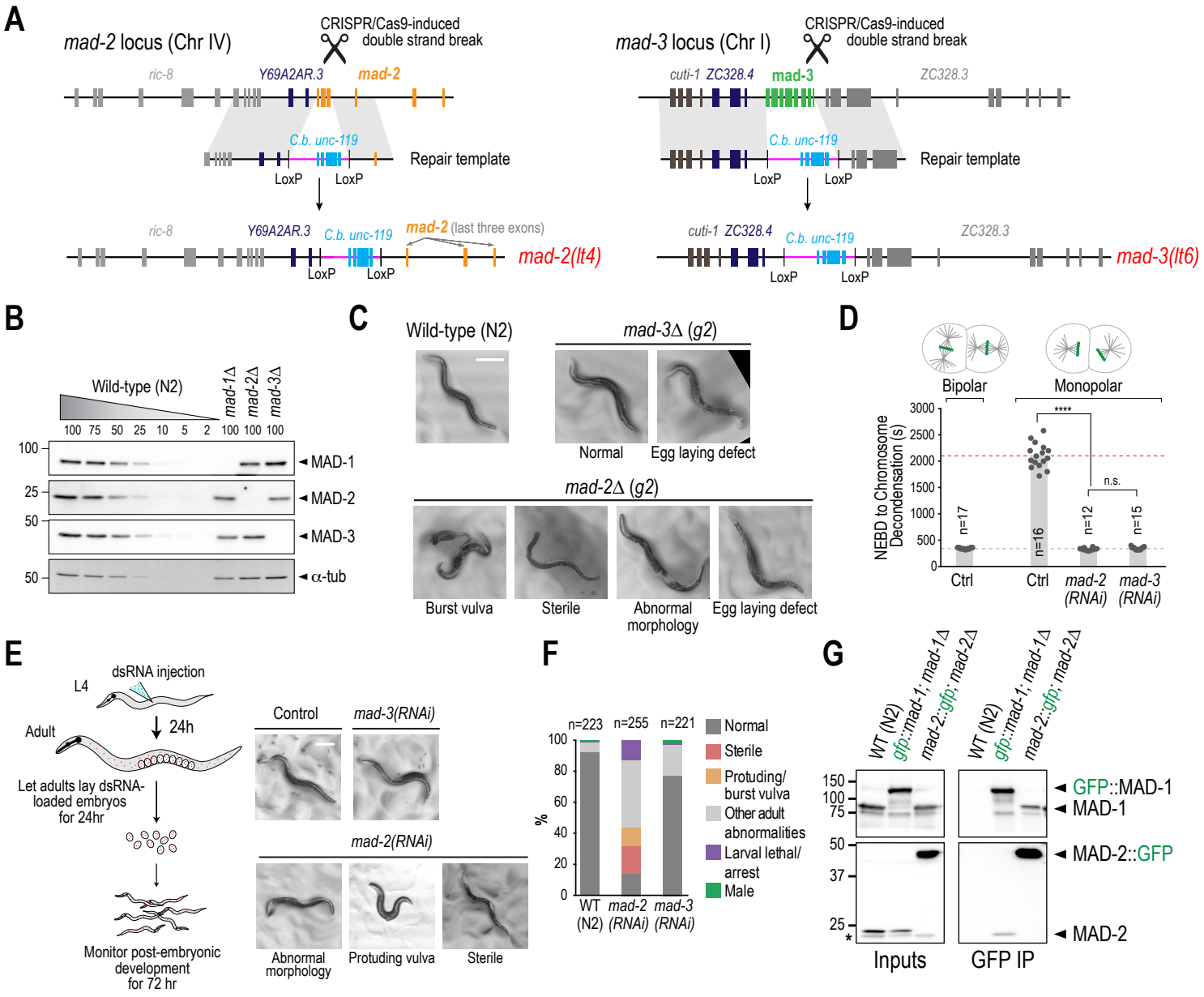

Figure S1. Generation of *mad-2*Δ and *mad-3*Δ worms and phenotypic analysis using RNAi-mediated depletion. (Related to Figure 1). **(A)** Schematic of CRISPR-Cas9-mediated generation of *mad-2* (*mdf-2*) and *mad-3* (*san-1*) null mutants. For the generation of these alleles, the Cas9-mediated dsDNA break was repaired using a template that replaced the coding sequences for *mad-2* and *mad-3* with *C. briggsae unc-119*. Editing was done in the background of an *unc-119(ed3)* mutant strain, which allowed for the selection of organisms that rescued the paralysis phenotype. In the case of *mad-2*, only the start codon and first 4 exons were deleted; the residual 3 exons in the *mad-2* deletion (which encode the last 93 amino acids of the 203 amino acid full-length protein) are not likely to generate a protein product. *mdf-2(lt4)* and *san-1(lt6)* are referred to as *mad-2*Δ and *mad-3*Δ, respectively. **(B)** Immunoblotting of indicated mutants with affinity-purified antibodies. *mad-1*Δ is the *mdf-1(gk2)* mutant, which deletes the entire *mad-1* genomic locus. α-tubulin was used as a loading control. **(C)** Examples of phenotypes observed for *mad-2*Δ and *mad-3*Δ worms for the indicated homozygous generation. Scale bar, 0.25 mm. **(D)** RNAi-mediated analysis of checkpoint signaling activity, performed as in *Fig. 1B,C*. Control bipolar and control monopolar data are the same as in *Fig. 1C*. *n* corresponds to the number of embryos analyzed for mitotic duration. Asterisks represent p<0.0001 from Mann-Whitney tests; non-significant (n.s.) is p>0.05. **(E) & (F)** RNAi-mediated analysis of phenotypes. Schematic in *(E)* indicates the experimental strategy. Images show representative phenotypes, and the graph in *(F)* depicts frequency of observed phenotypes. Scale bar, 0.25 mm. *n* corresponds to the number of adults scored for developmental defects. **(G)** Evidence that MAD2::GFP retains the ability to bind MAD-1. Lysates prepared from worms expressing either GFP::MAD-1 or MAD-2::GFP transgenes in the background of their respective null mutants were subjected to GFP immunopurification. Input lysates and immunoprecipitates were analyzed by immunoblotting with anti-MAD-1 (*top blots*) and anti-MAD-2 (*bottom blots*) antibodies. GFP::MAD-1 co-purified MAD-2 and MAD-2::GFP co-purified MAD-1. Asterisk marks a non-specific band detected in the lysate by the anti-MAD-2 antibody.

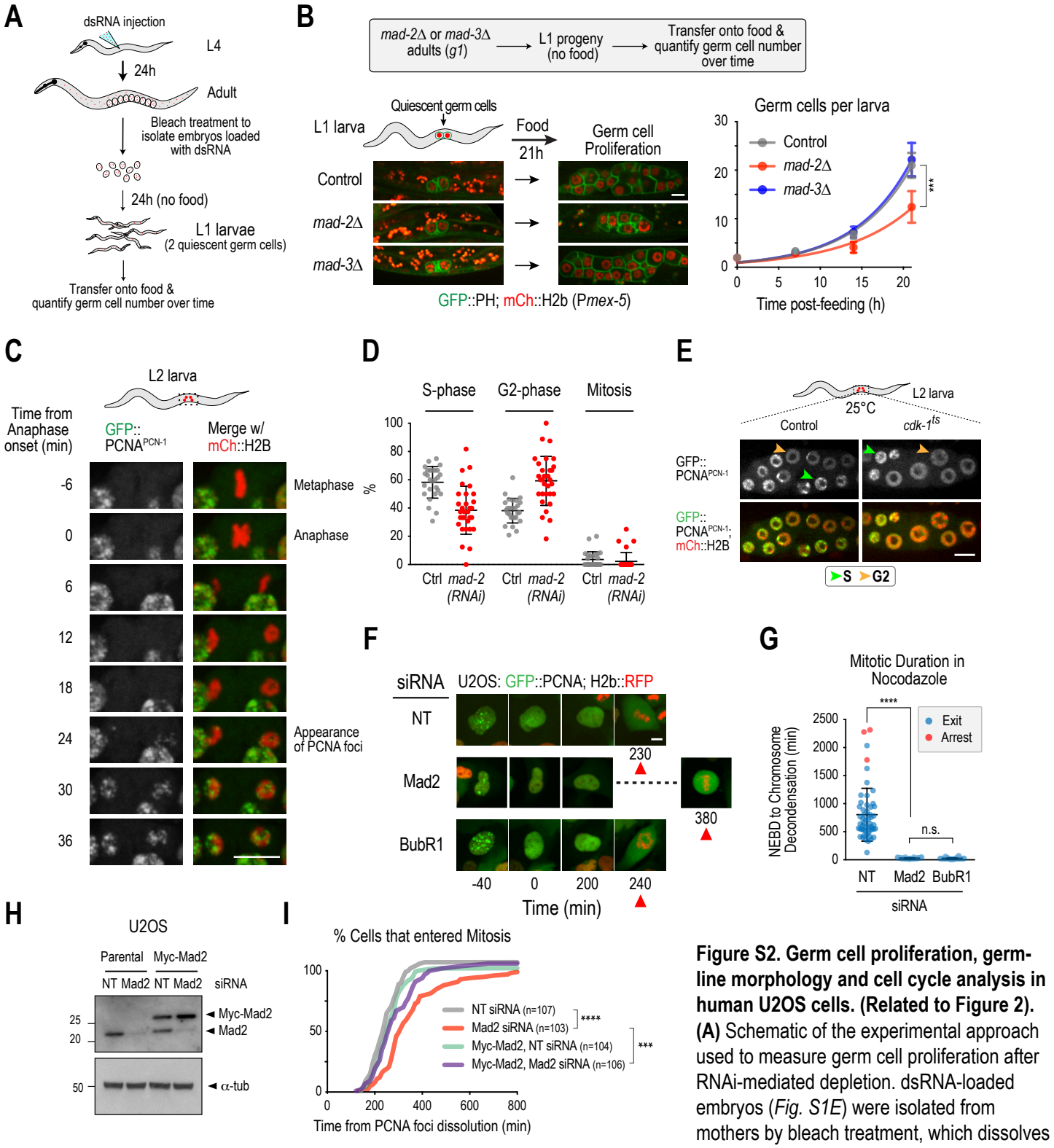

Figure S2. Germ cell proliferation, germline morphology and cell cycle analysis in human U2OS cells. (Related to Figure 2).
(A) Schematic of the experimental approach used to measure germ cell proliferation after RNAi-mediated depletion. dsRNA-loaded embryos (*Fig. S1E*) were isolated from mothers by bleach treatment, which dissolves the worm bodies without affecting the eggshell-protected embryos. Embryos were allowed to hatch in the absence of food, which results in synchronized L1 larvae with two quiescent germ cells. Larvae were transferred onto plates with food and the number of germ cells was quantified over time.
(B) Analysis of germ cell proliferation in L1 larval progeny of F1 homozygous *mad-2Δ* and *mad-3Δ* mutants. (*left*) Representative images of larvae expressing GFP::PH and mCherry::H2b under control of a germ cell-specific promoter (P*mex-5*), for the indicated conditions. (*right*) Plots of germ cell number over time. Note that the null mutants phenocopy the dsRNA-treated larvae in this assay (*Fig. 1C*). >16 larvae were quantified for each time point. Scale bar 5 µm. Error bars are 95% confidence intervals. Asterisks represent p=0.0002 from Mann-Whitney tests.

(figure legend continues on next page)

Figure S2 (contd.). Germ cell proliferation, germline morphology and cell cycle analysis in human U2OS cells. (Related to Figure 2).

(C) Evidence that germ cells have little-to-no G1 phase. Live imaging of a dividing germ cell expressing GFP::PCNA^{PCN-1} and mCherry::H2b shows appearance of PCNA foci, indicative of S-phase onset, 10-15 min after nuclear reformation. Scale bar, 5 μm.
(D) Cell cycle phase distribution of germ cells in control and *mad-2(RNAi)*. Data for G2-phase are the same as in *Fig. 2B*. Error bars are standard deviation.
(E) Representative images of L2 stage larvae expressing GFP::PCNA^{PCN-1} and mCherry::H2b, in the presence or absence of a weakening *cdk-1* mutation (*cdk-1^{ts}*). Experiments were done at the restrictive temperature of 25°C. Arrowheads point to S-phase (*green*) and G2 (*orange*) germ cells. Scale bar 5 μm.
(F) Example stills of the nuclear region from time-lapse movies of U2OS cells expressing GFP-PCNA and H2b-RFP. Specific conditions analyzed are indicated on the left. Time 0 is when PCNA foci were no longer observed in the nucleus and the red arrowhead points to when NEBD was observed. Scale bar, 10 μm.
(G) Analysis of spindle checkpoint signaling in U2OS cells. Cells were treated with the indicated siRNAs, incubated with nocodazole (0.2 μg/ml) and followed by time-lapse microscopy. Under these conditions, control cells exhibit a robust checkpoint-dependent mitotic arrest. Note that siRNA-mediated depletion of either Mad2 or BubR1 results in a similar checkpoint defect, validating functional inhibition of both proteins. The experiment was performed as indicated in *Fig.* 2E, except that images were acquired at 5 min intervals. Error bars are standard deviations. Asterisks represent $p<0.0001$ from Mann-Whitney tests; non-significant (n.s.) is $p>0.05$
(H) Immunoblot assessing Mad2 protein depletion efficiency in human U2OS cells transduced with a lentivirus expressing Myc-Mad2. NT is a non-targeting siRNA used as a control.
(I) Percent cells in mitosis as a function of time after PCNA foci dissolution for the indicated conditions. Myc-Mad2 suppressed the mitotic entry defect of Mad2 depletion, confirming specificity of the siRNA. **** represents $p<0.0001$ from Kolmogorov-Smirnov test; *** is $p=0.0003$.

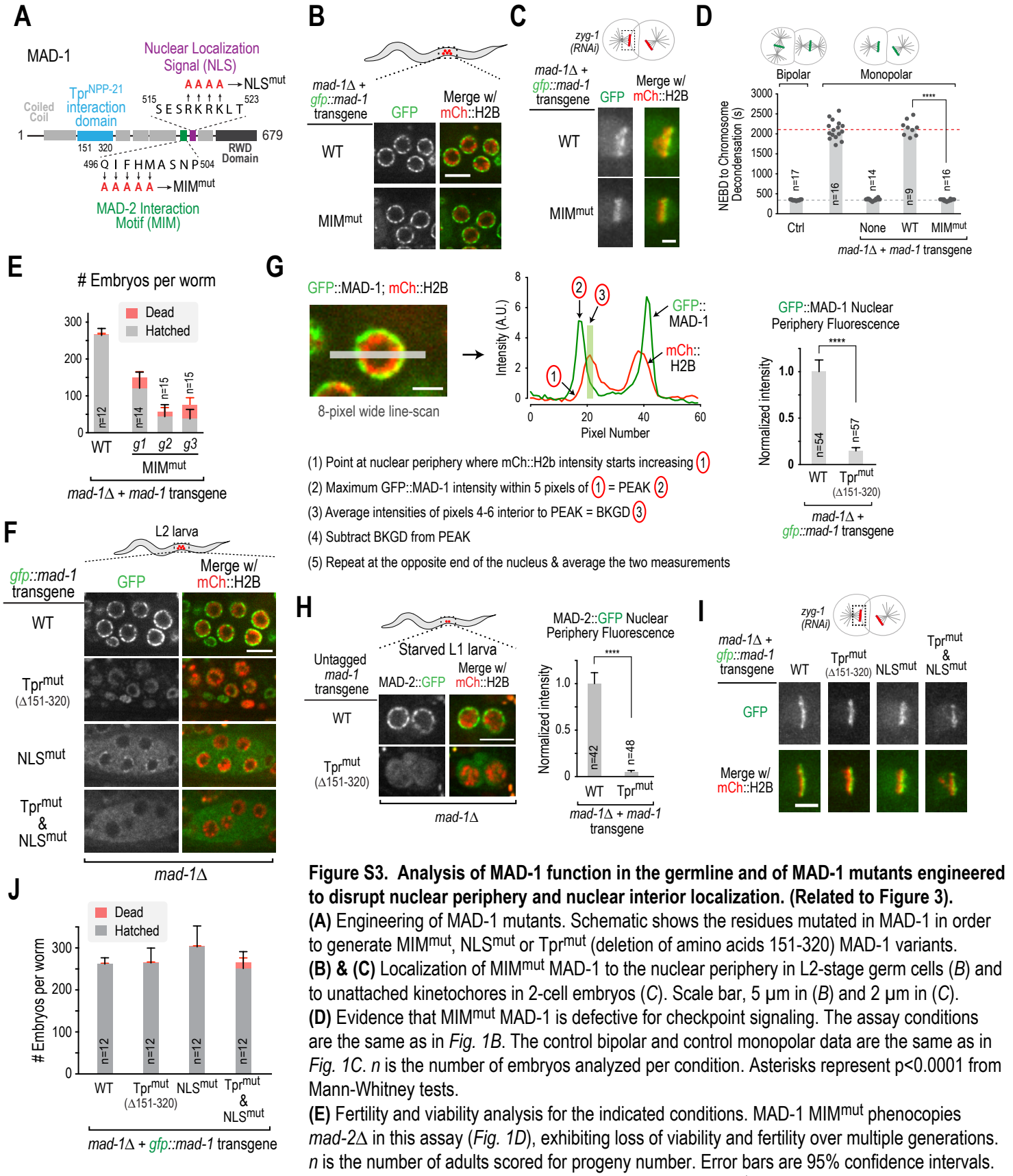

Figure S3. Analysis of MAD-1 function in the germline and of MAD-1 mutants engineered to disrupt nuclear periphery and nuclear interior localization. (Related to Figure 3).

(A) Engineering of MAD-1 mutants. Schematic shows the residues mutated in MAD-1 in order to generate MIM^{mut}, NLS^{mut} or Tpr^{mut} (deletion of amino acids 151-320) MAD-1 variants.

(B) & (C) Localization of MIM^{mut} MAD-1 to the nuclear periphery in L2-stage germ cells (*B*) and to unattached kinetochores in 2-cell embryos (*C*). Scale bar, 5 μm in (*B*) and 2 μm in (*C*).

(D) Evidence that MIM^{mut} MAD-1 is defective for checkpoint signaling. The assay conditions are the same as in *Fig. 1B*. The control bipolar and control monopolar data are the same as in *Fig. 1C*. *n* is the number of embryos analyzed per condition. Asterisks represent p<0.0001 from Mann-Whitney tests.

(E) Fertility and viability analysis for the indicated conditions. MAD-1 MIM^{mut} phenocopies *mad-2*Δ in this assay (*Fig. 1D*), exhibiting loss of viability and fertility over multiple generations. *n* is the number of adults scored for progeny number. Error bars are 95% confidence intervals.

(F) Images of indicated GFP-tagged MAD-1 mutants in the developing germline. The MAD-1 Tpr^{mut} cannot localize to nuclear pores and is diffuse in the nucleus, whereas NLS^{mut} is cytosolic with a small pool at nuclear pores. Combining both mutations (Tpr^{mut} & NLS^{mut}) results in a version of MAD-1 that is completely cytosolic. Scale bar, 5 μm.

(figure legend continues on next page)

Figure S3 (contd.). Analysis of MAD-1 function in the germline and of MAD-1 mutants engineered to disrupt nuclear periphery and nuclear interior localization. (Related to Figure 3).

(G) (*left*) Method used to quantify nuclear periphery localization of MAD-1 using an 8 pixel-wide line-scan. Scale bar, 2 μm. (*right*) Quantification of MAD-1 nuclear periphery localization. *n* is the number of nuclei quantified for MAD-1 nuclear periphery fluorescence. Error bars are 95% confidence intervals. Asterisks represent $p<0.0001$ from Mann-Whitney tests.
(H) Effect of Tpr^{mut} MAD-1 on localization of MAD-2 to the nuclear periphery in germ cells. MAD-2::GFP nuclear periphery localization was quantified as in (*G*), except that starved L1 larvae were used for this analysis as they exhibited robust MAD-2::GFP signal at nuclear pores. Scale bar, 5 μm. *n* is the number of nuclei analyzed per condition. Error bars are 95% confidence intervals. Asterisks represent $p<0.0001$ from Mann-Whitney tests.
(I) Localization of indicated MAD-1 variants to unattached kinetochores on monopolar spindles. At least 3 embryos were imaged per condition and a representative embryo is shown. Scale bar, 5 μm.
(J) Fertility/viability analysis for the indicated conditions. *n* is the number of adults scored for progeny number. Error bars are 95% confidence intervals.

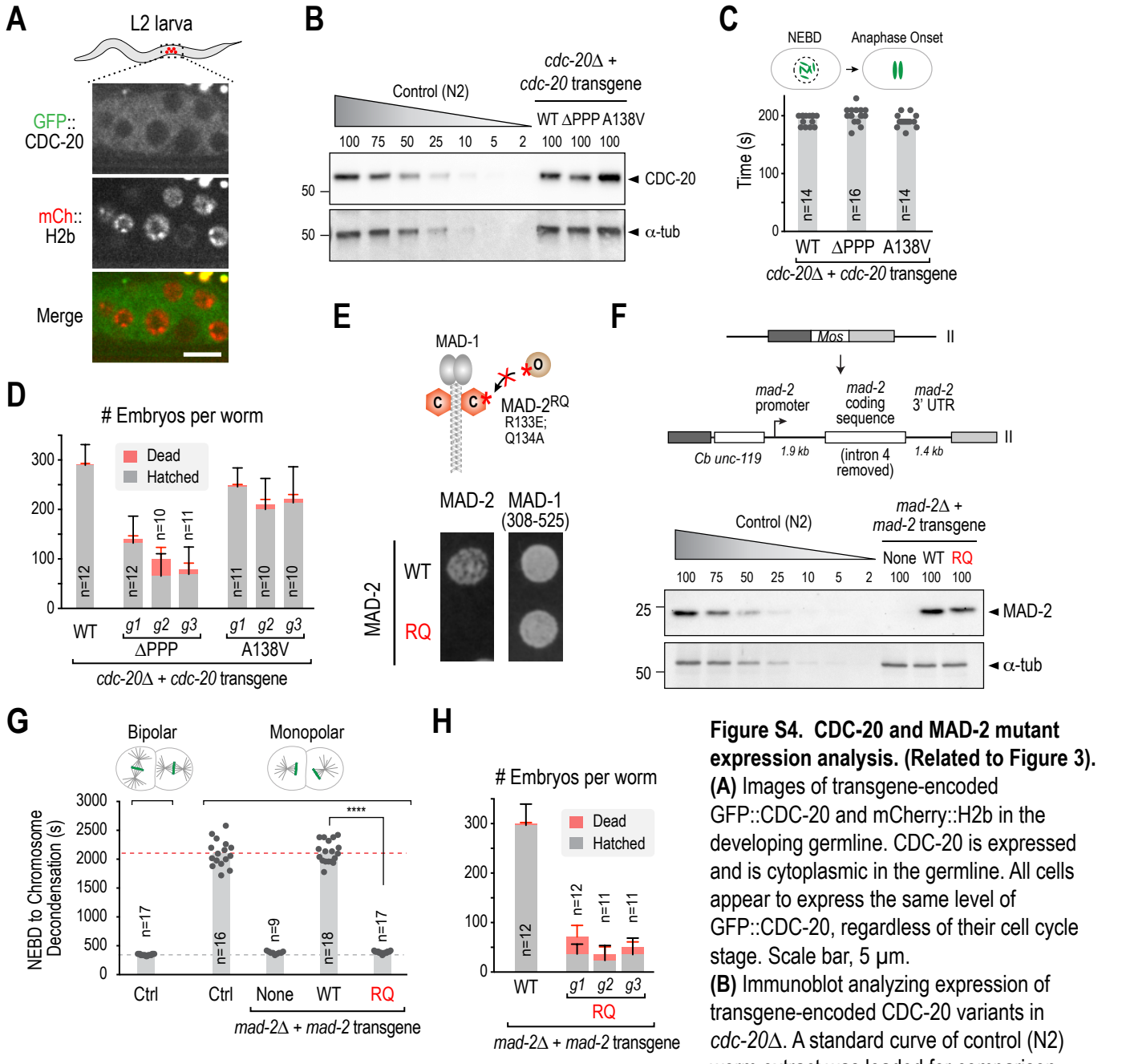

Figure S4. CDC-20 and MAD-2 mutant expression analysis. (Related to Figure 3).
(A) Images of transgene-encoded GFP::CDC-20 and mCherry::H2b in the developing germline. CDC-20 is expressed and is cytoplasmic in the germline. All cells appear to express the same level of GFP::CDC-20, regardless of their cell cycle stage. Scale bar, 5 µm.
(B) Immunoblot analyzing expression of transgene-encoded CDC-20 variants in *cdc-20Δ*. A standard curve of control (N2) worm extract was loaded for comparison.
(C) NEBD-anaphase onset timing in one-cell embryos for the indicated conditions. Both CDC-20 mutants rescue mitotic timing to the same extent as CDC-20 wild-type, indicating that activate the APC/C normally. *n* is the number of embryos analyzed.
(D) Fertility/viability analysis for the indicated conditions. CDC-20 ΔPPP, but not A138V, phenocopies *mad-2Δ* in this assay (*Fig. 1D*), exhibiting loss of viability and fertility over multiple generations. *n* is the number adults scored. Error bars are the 95% CI.
(E) (*top*) Schematic of MAD-2 dimerization-disrupting RQ mutant (R133E, Q134A) and (*bottom*) yeast 2-hybrid analysis of MAD-2 interaction with itself and with MAD-1. The MAD-2 RQ mutant blocks self-interaction but not the interaction with MAD-1.
(F) (*top*) Schematic of *mad-2* transgene insertion system used to engineer mutations into MAD-2. The transgene includes the genomic *mad-2* locus with the exception of intron 4, which was removed. (*bottom*) Immunoblot of the MAD-2 variants expressed from single copy transgene insertions in the background of *mad-2Δ*. A standard curve of control (N2) worm extract was loaded for comparison. α-tubulin serves as a loading control.
(G) & (H) Checkpoint signaling (*G*) and fertility and viability analysis (*H*) for wild-type versus RQ mutant MAD-2 in *mad-2Δ*. Checkpoint activity analysis was performed as in *Fig. 1B*. Control bipolar and control monopolar data are the same as in *Fig. 1C*. Consistent with work in other systems, MAD-2 RQ is defective in checkpoint signaling. *n* is the number of embryos analyzed (G) or the number of adults scored (*H*). Error bars are 95% confidence intervals. Asterisks represent p<0.0001 from Mann-Whitney tests.

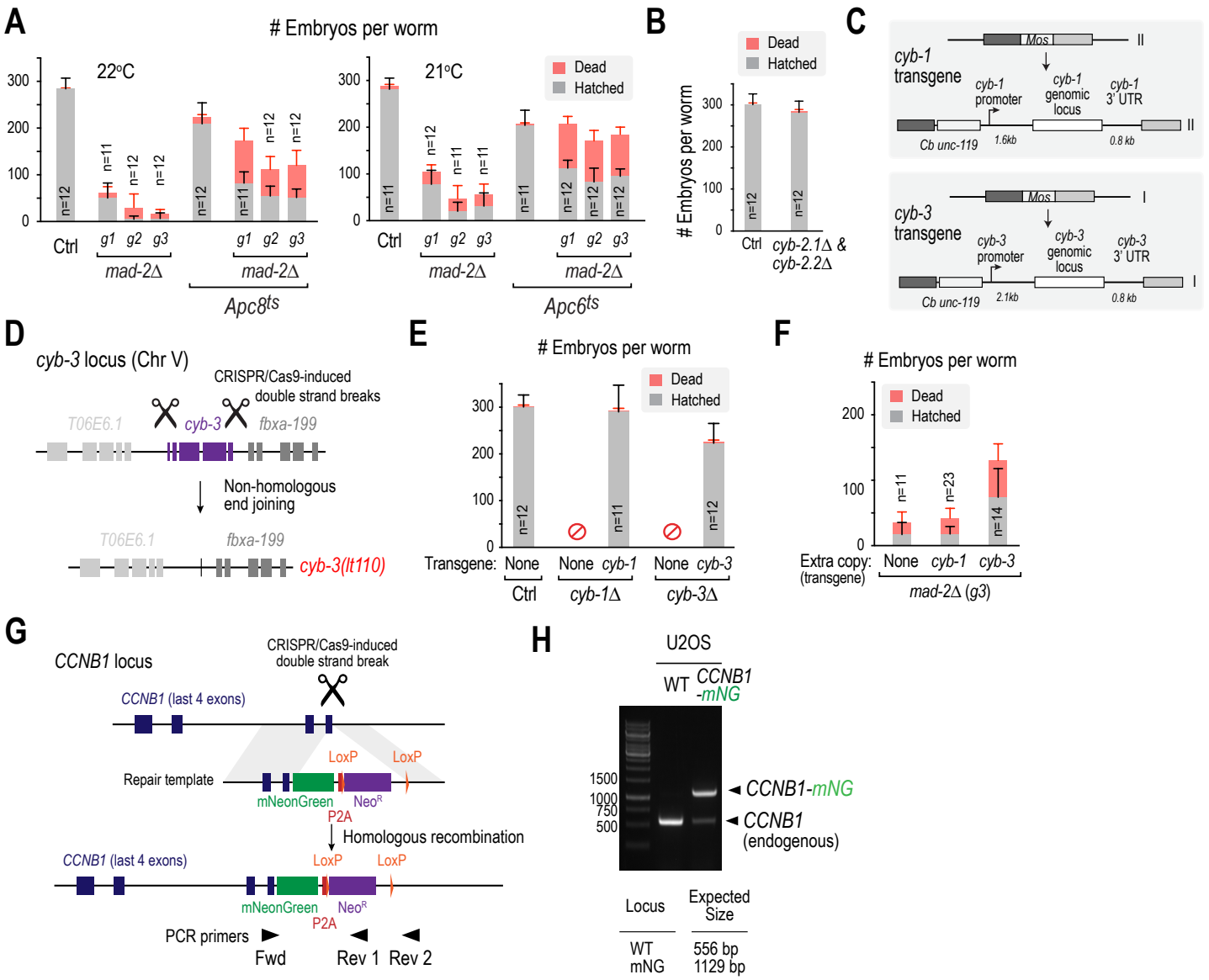

Figure S5. Analysis of fertility/viability of *Apc6ts* and *Apc8ts* mutants, characterization of cyclin B isoforms and generation of cyclin B1-mNeonGreen U2OS cells. (Related to Figure 4).

(A) Analysis of fertility/viability for the indicated conditions. *Apc6ts* and *Apc8ts* mutants at semi-permissive temperature (22°C and 21°C respectively) partially suppress fertility defect of *mad-2*Δ; significant embryonic lethality is still observed. *n* is the number adults scored for progeny number. Error bars are 95% confidence intervals.

(B) Fertility/viability analysis for a *cyb-2.1*Δ;*cyb2.2*Δ double mutant. Unlike nulls for *cyb-1* or *cyb-3*, the double *cyb-2* null is viable and fertile. *n* is the number of adults scored for progeny number. Error bars are 95% confidence intervals.

(C) Schematics of single copy transgene insertions engineered for *cyb-1* and *cyb-3*.

(D) Schematic describing generation of the *cyb-3(lt110)* null mutant by CRISPR/Cas9, referred to as *cyb-3*Δ.

(E) Evidence for functionality of *cyb-1* and *cyb-3* transgene insertions, based on rescue of lethality of the respective null mutants. *cyb-1*Δ = *cyb-1(gk35)* and *cyb-3*Δ= *cyb-3(lt110)*. Control values are the same as in (*B*). Error bars are 95% confidence intervals.

(F) Fertility/viability analysis for the indicated conditions. An extra transgene-encoded dose of CYB-3, but not CYB-1, partially suppresses fertility and viability phenotype of *mad-2*Δ(G3) worms. *n* is the number adult worms scored for progeny number. Error bars are 95% confidence intervals.

(G) – (H) Generation of the *in situ* mNeongreen-tagged cyclin B1 U2OS cell line. (*G*) Schematic describing the CRISPR-Cas9 strategy used to *in situ* tag the *CCNB1* locus with the coding sequence for mNeongreen. (*H*) Genotyping of the *CCNB1-mNG* U2OS line using PCR with a mixture of the 3 primers depicted in the schematic. Clones were first screened by immunoblotting (see *Fig. 4D*). In U2OS cells, chromosome 5 containing the *CCNB1* locus is present in 4 copies (Janssen and Medema, 2013). While the immunoblotting suggests nearly all of the Cyclin B1 is mNeongreen-fused in the isolated clone, the genotyping indicates that an unedited *CCNB1* locus is still present.

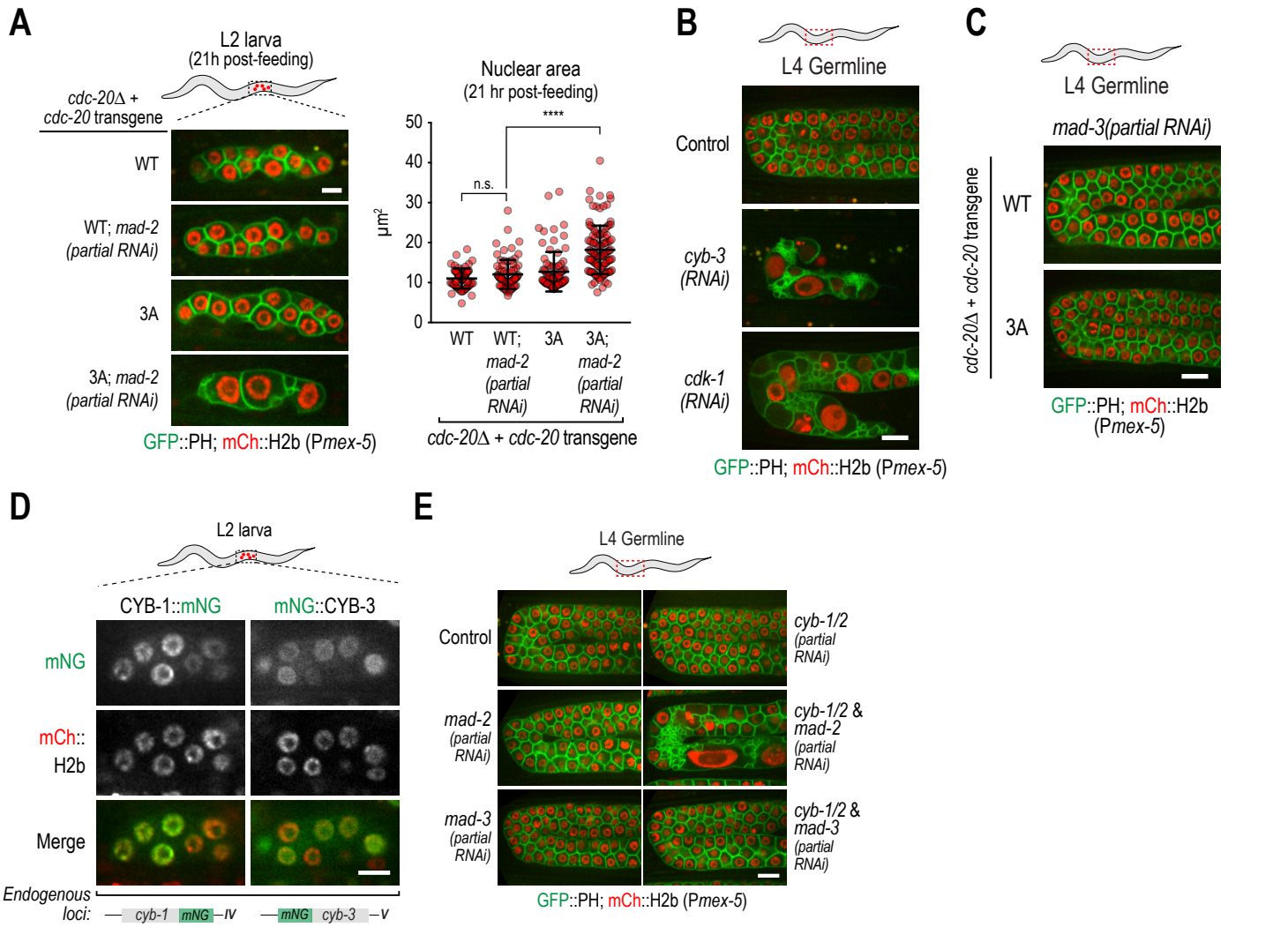

Figure S6. CDC-20 phosphorylation mutant analysis and characterization of cyclin B isoform expression in germ cells. (Related to Figure 5).

(A) Representative images (*left*) and quantification of nuclear area (*right*) of L2-stage germlines expressing GFP::PH and mCherry::H2b under the indicated conditions. Scale bar, 5 μm. Error bars are standard deviations. Asterisks represent p<0.0001 from Mann-Whitney tests; non-significant (n.s.) is p>0.05.

(B), (C) & (E) Representative images of L4-stage germlines expressing GFP::PH and mCherry::H2b for the indicated conditions. Scale bar, 10 μm.

(D) Localization of *in situ* mNeogreen-tagged CYB-1 and CYB-3 in a strain also expressing mCherry-tagged H2b. Note that both cyclin B isoforms are expressed in germ cells, despite *cyb-1/2(RNAi)* alone not having a significant effect on mitotic entry (*Fig. 4C*). Scale bar, 5 μm.

Supplemental Tables

Table S1. CRISPR/Cas9 targeting sequences used in this study. (Related to STAR Methods).

Target gene no.	**Name**	**Allele generated**	**Target sequence(s) (5'→3')**
Y69A2AR.30	*mad-2*	*mad-2*Δ	GCCAAATTCCCCAGTTTTAG
ZC328.4	*mad-3*	*mad-3*Δ	GCAGTTGCACGCACCATCGA
Y69A2AR.30	*mad-2*	*mad-2::gfp*	CACGAATGTACAGTACAAGG AACAGACAAAAATTATTCGG
ZC168.4	*cyb-1*	*cyb-1::mNeonGreen*	ATGCGTCCACTTTTGCATTC
T06E6.2	*cyb-3*	*mNeonGreen::cyb-3*	TGAAGTCAGGTCGACATTCT
T06E6.2	*cyb-3*	*cyb-3*Δ	TCAGGTCGACATTCTTGGCC GTTATGGGTATGAGAGCATT
CCNB1	Cyclin B1	Cyclin B1-mNeonGreen	TTTAGCCAAGGCTGTGGCAA

Table S2. Primers for dsRNA production. (Related to STAR Methods).

Gene no.	Name	Oligonucleotide (5'→3') #1	Oligonucleotide (5'→3') #2	Template	Conc. (mg/ml)
F59E12.2	*zyg-1*	TAATACGACTCACTATAGGAACGAAATTCCCTTGAGCTG	AATTAACCCTCACTAAAGGTGGACGGAAATTCAAACGAT	Genomic DNA	1.5
Y69A2AR.30	*mad-2*	TAATACGACTCACTATAGGGTGAACTGACGTCGAGAATGAG	AATTAACCCTCACTAAAGGACGGATGTAAAGACACAAAACG	cDNA	2.1
ZC328.4	*mad-3*	TAATACGACTCACTATAGGCGAAGAACTTCAAAACCTGGA	AATTAACCCTCACTAAAGGTTTGTCGGTCCAGATCCTTC	Genomic DNA	1.5
C50F4.11	*mad-1*	TAATACGACTCACTATAGGAAGCGAAGTTGGCTGAAAAA	AATTAACCCTCACTAAAGGAGCATCCTCAAGTCGTTCGT	Genomic DNA	1.7
ZC168.4 Y43E12A.1 H31G24.4 (*)	*cyb-1 & cyb-2*	TAATACGACTCACTATAGGTGGAATTTCAGCTATGTGAGAG	AATTAACCCTCACTAAAGGAGAGGCTCCGAGCTGTTTG	Genomic DNA	1.2
T06E6.2	*cyb-3*	TAATACGACTCACTATAGGGCGAGGCGACATGGAAGAATA	AATTAACCCTCACTAAAGGTGTGCAAGACGAAGAATGTTG	Genomic DNA	1.5
T05G5.3	*cdk-1*	TAATACGACTCACTATAGGGTCGTAGATCAGCAAACCCTGA	AATTAACCCTCACTAAAGGACCTTCCGCTCGAAACTCTT	Genomic DNA	0.9
K06A5.7	*cdc-25.1*	AATTAACCCTCACTAAAGGCCATCATGCGACTTCCAAAA	TAATACGACTCACTATAGGAAAAGTAATTTTCTGGATAACTTCAAA	Genomic DNA	1.8
C05C8.9	*hyls-1*	AATTAACCCTCACTAAAGGTGGCAAATTTTACCACTGAAA	TAATACGACTCACTATAGGTGATATCTTGTGACCGGATCA	Genomic DNA	2.5

(*) Due to high sequence homology, a single dsRNA is predicted to hit *cyb-1* and the two *cyb-2* isoforms.